Chinese Chemical Letters 31 (2020) 2263–2267

Contents lists available at ScienceDirect

Chinese Chemical Letters

journal homepage: www.elsevier.com/locate/cclet

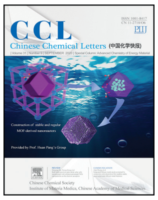

Communication

Morphology and size controlled synthesis of Co-doped MIL-96 by different alkaline modulators for sensitively detecting alpha-fetoprotein

Chaonan Gu[a], Jingjing Li[c], Guang Yang[a], Liming Zhang[a], Chun-Sen Liu[a,*], Huan Pang[b,*]

[a] *Henan Provincial Key Laboratory of Surface & Interface Science, Zhengzhou University of Light Industry, Zhengzhou 450002, China*
[b] *School of Chemistry and Chemical Engineering, Guangling College, Yangzhou University, Yangzhou 225009, China*
[c] *School of Chemistry and Chemical Engineering, Henan University of Technology, Zhengzhou 450001, China*

ARTICLE INFO

Article history:
Received 31 December 2019
Received in revised form 23 January 2020
Accepted 12 February 2020
Available online 21 February 2020

Keywords:
Morphology/size
MIL-96
Modulator
Aptasensor
Alpha-fetoprotein

ABSTRACT

This work introduces a simple and facile approach for the morphology and size controlled synthesis of Co-doped MIL-96. By using different bases as modulators, Co-doped MIL-96 was obtained with sizes that varied from 5 μm to 300 nm, and four different morphologies, including hexagonal prism, icosahedron, hexagonal spindle and ellipsoid. Among these, nano-sized Co-doped MIL-96 with an ellipsoid morphology exhibited the highest electroactive surface area and good conductivity as well as the best electrochemical sensing performance towards α-fetoprotein.

Metal-organic frameworks (MOFs) have attracted significant interest as an emerging class of multifunctional porous materials. Due to their diverse structures, tunable pore sizes, large specific surface areas and large numbers of active sites, MOFs are widely used in gas storage and separation [1,2], catalysis [3–6], sensing [7,8], drug delivery [9] and energy storage [10,11]. Recently, studies have shown that control of the size and morphology of MOFs is essential for determining their chemical, physical and biological characteristics [6,12–15]. Our group was the first to demonstrate the effect of nanocrystal planes on the electrocatalytic activity of [$Cu(btc)_2$] nanocrystals with different morphologies (nanocubes, truncated cubes, cuboctahedrons and octahedrons) in glucose oxidation [14]. Morsali's group has demonstrated that nano TMU-34 MOF obtained using the ultrasonic method displayed much better sensing performance towards cation than its bulk MOFs counterparts [15]. Thus, controlling the synthesis of MOFs with specific shapes and sizes, which requires precise control of their nucleation and growth, is of great importance for the optimization of their performance [16]. The use of surfactants, monocarboxylic acids, ligands and other additives are common strategies for regulating the morphology and size of MOFs [17–20]. However, systemically and regularly controlling the morphology and size of MOFs is still a significant challenge due to their diverse structures and complex nucleation and growth processes [21]. Effective methods for controlling the growth of MOFs are still needed for the optimization of their performance.

Coordination modulation by adding a modulator directly is an enticing approach for tuning the crystal morphology and size of MOFs [22,23]. Among these modulators, an acid or base with the same or different functional groups as the organic ligands can act as a coordination regulator that tunes the coordination directly between the metal ion and the organic ligand, impacting the size and the morphology of the MOFs [24–26]. MIL-96, which has diverse and controllable particle sizes and shapes, has been widely studied by researchers since its initial report [27,28]. However, few studies have examined the relationship between the characteristics of MIL-96 and its specific crystal planes and size [29]. Additionally, MIL-96 has potential applications in developing sensor devices due to its high porosity, specific surface area, low toxicity and good water stability [30,31]. In recent years, many advantages of sensors based on electrochemical technologies have attracted more and more attentions [32]. Unfortunately, most MOFs have poor conductivity, which limits their application in electrochemistry [33]. Doping transition metals into MOFs and adjusting their morphology and size may be effective methods to address this limitation.

In the current work, a simple coordination modulation strategy was developed to control the synthesis of Co-doped MIL-96. Co-

---

[*] Corresponding authors.
E-mail addresses: chunsenliu@zzuli.edu.cn (C.-S. Liu), panghuan@yzu.edu.cn (H. Pang).

https://doi.org/10.1016/j.cclet.2020.02.044
1001-8417/

doped MIL-96 with different morphologies (hexagonal prism, icosahedron, hexagonal spindle and ellipsoid) was successfully prepared through four different alkaline reagents, including tetramethylammonium hydroxide (TMAH), *N*,*N*'-dimethylacetamide (DMA), *N*,*N*'-dimethylformamide (DMF) and triethylamine (TEA), as cosolvents to modulate the coordination. The as-obtained materials are labelled M1, M2, M3 and M4, respectively. Scheme 1 summarizes the synthetic process and the morphologies and size of the materials obtained in this study. The effects of the morphology and size on the properties of the material were studied. The results showed that nano-sized Co-doped MIL-96 with an ellipsoid morphology exhibited the highest electroactive surface area and conductivity, as well as the best electrochemical sensing performance towards alpha-fetoprotein (AFP).

Firstly, we synthesized MIL-96 in the condition without adding $Co(NO_3)_2 \cdot 6H_2O$ and any cosolvent. The SEM image (Fig. S2a in Supporting information) shows the MIL-96 had a non-uniform morphology and size. In addition, a series of different doping amounts of Co-doped MIL-96 were synthesized by adding $Co(NO_3)_2 \cdot 6H_2O$ with a different molar ratio to $Al(NO_3)_3 \cdot 9H_2O$ (1:4, 1:1 and 1:0.25) in the system without any cosolvent (The as-obtained materials are labelled $M_{1:4}$, $M_{1:1}$ and $M_{1:0.25}$, respectively). As can be seen from Figs. S2b-d (Supporting information), compared with MIL-96, their morphology has changed. In order to study the influence of the Co doping on the materials, a preliminary study on the application potential of the electrochemical aptasensor bioplatform for the prepared materials (Fig. S3 in Supporting information). The test results obtained for MIL-96, $M_{1:4}$, $M_{1:1}$ and $M_{1:0.25}$ are shown in Table S1 (Supporting information) and can further compare their performance according to Fig. S4 (Supporting information). Fig. S4 show that the effect of Co doping on the conductivity of the material is obvious. However, there was no significant change in the load of the aptamer in the aptasensors and the amount of AFP bound to the aptamer. Based on the above results, although $M_{1:0.5}$ has slightly better conductivity than $M_{1:1}$, the morphology and size of $M_{1:1}$ are more uniform. After that, under the condition of Al^{3+}:Co^{2+} molar ratio was 1:1, we further adjusted the morphology and size of the material by introducing the cosolvent. M1, M2, M3 and M4 were obtained by adding different alkaline solvents, respectively, and further study was performed on them.

The bonding properties of the as-prepared samples were verified by Fourier transform infrared (FTIR). Fig. S5 (Supporting information) shows the FTIR spectra of H_3BTC and the as-obtained materials. Similar spectra were observed for M1, M2, M3 and M4, demonstrating that they have the same bonding properties. Compared to H_3BTC, the disappearance of the C—OH absorption at 1278 cm^{-1} for Co-doped MIL-96 indicates that the H_3BTC ligand is deprotonated and coordinates to the metal center. The structural characterization was further confirmed by powder X-ray diffraction (PXRD). The PXRD patterns of M1, M2, M3 and M4 are shown in Fig. 1a. It can be seen that M1, M2, M3 and M4 show similar patterns to simulated MIL-96 [34], indicating that the Co doping does not cause framework changes of MIL-96. Fig. 1b shows the crystal structure of MIL-96. The effects of the four different cosolvents as modulators on the morphology and size of the materials were monitored by scanning electron microscopy (SEM). The SEM image shows that M1, obtained with TMAH as a cosolvent, has a hexagonal prism shape and an average diameter of about 4 μm (Fig. 1c). M2, synthesized using DMA as a cosolvent, displays an icosahedron morphology with an average diameter of about 5 μm. However, some octadecahedron particles with an average size of about 3 μm were also observed under these conditions (Fig. 1d). M3, obtained using DMF as a cosolvent, has a hexagonal spindle shape with a diameter of about 3 μm (Fig. 1e). When TEA was used as a cosolvent, an elliposoid shape was obtained for M4 and its edges became smooth. In addition, its average diameter decreased to 300–400 nm (Fig. 1f). Consequently, it can be seen that the alkaline reagent influence significant the morphology and size of the materials. As a cosolvent for dissolving H_3BTC, alkaline reagent can accelerate the deprotonation process of H_3BTC [35] thus promoting the formation of MOFs; the different influence of the alkaline reagent on the deprotonation process of H_3BTC lead to different nucleation rates and crystal plane growth.

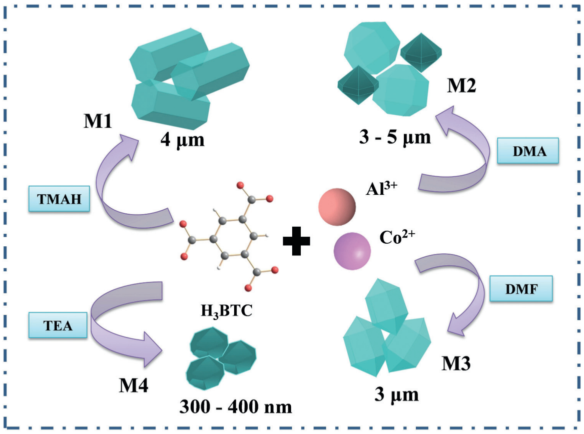

Scheme 1. Preparation process of morphology and size-controllable synthesis of Co-doped MIL-96.

The morphology of M4 was further characterized by transmission electron microscopy (TEM) (Figs. 2a and b). The TEM energy dispersive spectroscopy (EDS) mapping shows that the distribution of C, O, Al and Co is uniform (Figs. 2c–h), indicating that the successful doping of Co into the product. X-ray photoelectron spectroscopy (XPS) was employed to analyze the elemental composition and valence state of the Co-doped MIL-96. The main peaks in the survey scan spectrum (Fig. 3a) occur at 284.45 eV, 531.03 eV, 76 eV and 781.93 eV, which can be attributed to the C 1s, O 1s, Al 2p and Co 2p, respectively. M1, M2, M3 and M4 have similar survey scan spectra, demonstrating that they have the same elemental composition. Table S2 (Supporting information) shows the atomic percentage of each element. To further characterize the presence and states of Co in the material, we analyzed the high-resolution Co 2p spectra of the four materials. As shown in Fig. 3b, the Co 2p region of these materials shows two typical peaks at about 781 eV and 796 eV that characteristic of Co $2p_{3/2}$ and Co $2p_{1/2}$, respectively, and two shake-up satellites (identified as "Sat.") at about 786 and 802 eV, which may be associated with the Co^{2+} [36]. These results indicate that a Co^{2+} species is present in the materials. In addition, we studied the thermal stability of the materials. The thermogravimetric analysis (TGA) curve (Fig. S6 in Supporting information) shows that there is no significant difference between the thermal stability of Co-doped MIL-96 and that of the previously reported MIL-96 [37], indicating that the framework is not affected by the Co doping. However, the final remaining weights of M1 (36.16%), M2 (37.95%), M3 (36.87%) and M4 (37.61%) are higher than the reported value (30.5%) [28]. This result is due to the change in the composition of the material due to the Co doping.

The electrochemical performance of M1, M2, M3 and M4 were characterized by cyclic voltammetry (CV) in 0.1 mol/L PBS containing 5 mmol/L $[Fe(CN)_6]^{3-/4-}$ as probes. The response changes of the CV curve of the AE and the AE modified with the four materials are shown in Fig. S7 (Supporting information). It can be seen that the modified AE has a decreased peak current compared to AE. This result shows that the modification of the material hinders the transfer of electrons at the AE surface. The

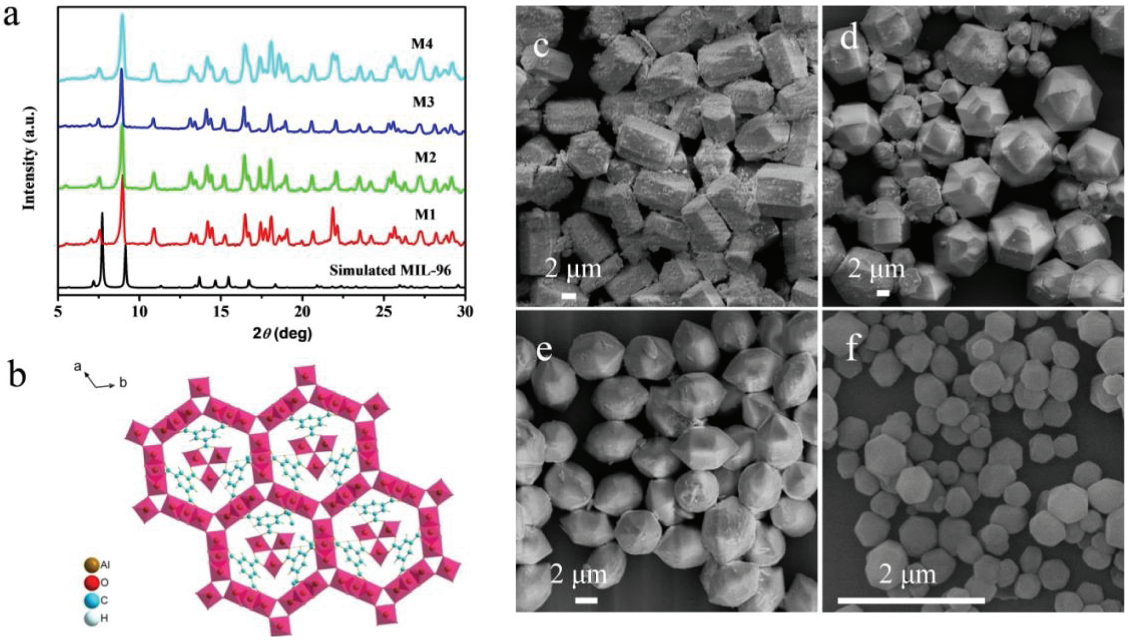

Fig. 1. (a) PXRD patterns of the M1, M2, M3 and M4. (b) The crystal structure of MIL-96. (c-f) SEM images of the M1, M2, M3 and M4.

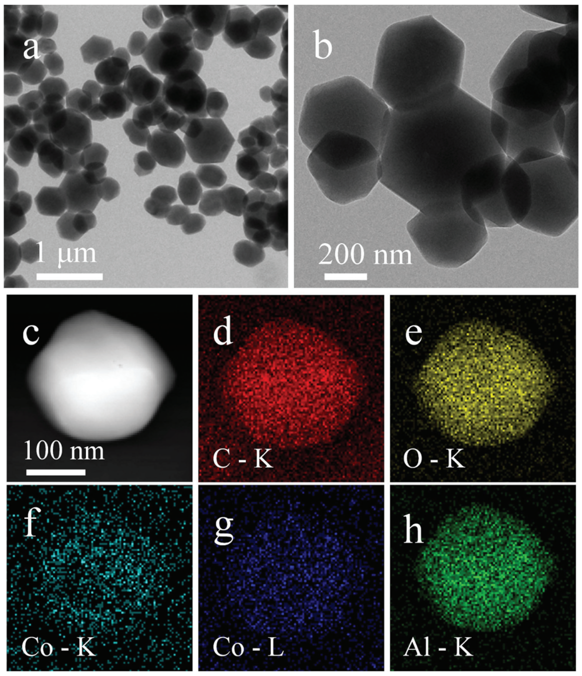

Fig. 2. (a) Low-magnitude and (b) high-magnitude TEM image of M4. (c-h) EDS elemental mapping images of M4: C, O, Co of K, Co of L and Al of K.

electroactive surface area (A) of the modified electrodes were estimated from the CV results using the Randles-Sevcik equation [38]:

$$I_p = 2.69 \times 105\ (n^{3/2})\ A\ D^{1/2}\ \nu^{1/2}\ C \qquad (1)$$

where I_p equals I_{pc}, for $Fe(CN)_6^{3-}$, n = 1, D = 6.7 × 10^{-6} cm^2/s, ν is the scan rate of the CV measurment and C is the concentration of the probe molecule in the solution (mol/cm^3). The calculated A values for M1/AE, M2/AE, M3/AE, M4/AE were 0.0742, 0.0793, 0.0810, 0.0895 cm^2, respectively. Among the four materials with different morphologies and sizes, the nano-sized M4 has the highest electroactive surface area.

Subsequently, the potential for the application of the as-obtained materials in the bioplatforms of electrochemical aptasensors was studied. The performance of aptasensors constructed using M1, M2, M3 and M4, which have different morphologies and sizes, was confirmed using EIS. The measured EIS spectra are shown in Fig. S8 (Supporting information). As the measurement proceeds, the R_{ct} value increases continuously. This trend is due to the modification of the surface of the electrode as the aptamer is adsorbed and the G-quadruplex is formed by the combination of the aptamer strands and AFP to further prevent electron transfer [39]. The R_{ct} values obtained for the four materials are shown in Table S3 (Supporting information). To analyze the performance of the four aptasensors, we compared their ΔR_{ct} values in Fig. S9 (Supporting information). As shown in Fig. S9 (Supporting information), the order of $R_{ct,materials}$-$R_{ct,AE}$, is: M1 > M3 > M4 > M2. This means the order of the electron transfer ability of the four materials is M2 > M4 > M3 > M1. Combined with the Co atomic% of the four materials in Table S2, the result can once again prove that the higher the doping amount of Co, the better the electrochemical performance of the material. The highest amount of the aptamer is immobilized on M4 because its smaller size is more favorable for loading the aptamer [40]. Moreover, among the four aptasensors, the ΔR_{ct} value calculated from $R_{ct,AFP}$ - $R_{ct,Apt}$ of the M4-based aptasensor is the highest, indicating that it has the best detection capabilities for AFP. Based on the results above, the M4-based aptasensor was selected for the further detection of AFP.

To further analyze the sensitivity of the selected aptasensor, EIS was carried out with different concentrations of AFP (0.001–0.5 ng/mL) using the aptasensor. As shown in Fig. 4a, the impedance increased gradually with increasing AFP concentration. This trend is due to a continuous increase in the AFP specifically recognized by aptamers, which form a thicker layer to block electron transport. Fig. 4b shows the change in ΔR_{ct} with AFP concentration. When the concentration reaches 0.1 ng/mL, the change in ΔR_{ct} stabalizes. A linear relationship is obtained between the ΔR_{ct} and the logarithm value of the AFP concentration (ΔR_{ct} = 2.142 + 0.587 $\log C_{AFP}$) with a correlation coefficient of 0.993. The limit of

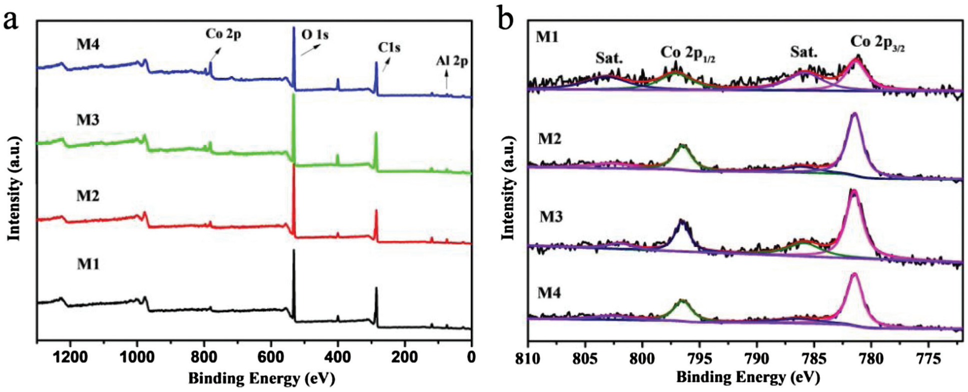

Fig. 3. (a) XPS survey scan spectra of M1, M2, M3 and M4. (b) High resolution XPS scan of M1, M2, M3 and M4 samples in Co 2p region.

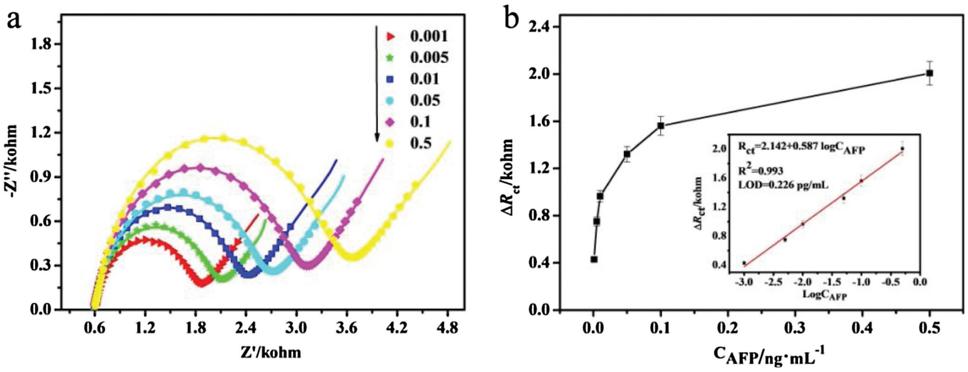

Fig. 4. (a) EIS responses of Apt/M4/AE with different concentrations of AFP. (b) Dependence of ΔR_{ct} on the concentration of AFP (Inset: the linear parts of the calibration curves).

detection (LOD) calculated based on the linear regression equation is 0.226 pg/mL (S/N = 3).

Furthermore, the reproducibility, selectivity and stability of the fabricated aptasensor for the detection of AFP were also examined (Fig. S10 in Supporting information). Fig. S10a exhibited a similar measurement results of the five modified electrodes were employed to detect 0.001 ng/mL AFP. The ΔR_{ct} values measured by five different electrodes with a relative standard deviation (RSD) of 0.88%. Fig. S10b shows that the aptasensor's recognition of AFP is much higher than other cancer markers (carcinoembryonic antigen (CEA), human serum albumin (HSA), and human immunoglobulin G (IgG) and lysozyme), revealing the prepared aptasensor has good selectivity for AFP. Fig. S10c shows the ΔR_{ct} values of the prepared aptasensor consistently test for 15 days. The RSD of measurements is calculated to be 0.82%. It is proved that the prepared aptasensor has good stability within a certain error range. And a real sample analysis was performed using healthy human serum (Table S4 in Supporting information), the recovery and the RSD range from 96% to 103%, 0.63%–3.38%, respectively. These results show the value of the fabricated aptasensor in this potential application.

In conclusion, a simple and facile approach for the controlled synthesis of Co-doped MIL-96 with varied morphology and size was developed by using different cosolvents TMAH, DMF, DMA and TEA as modulators. The as-obtained materials presented morphology/size-dependent electrochemical performance and the application potential of the as-obtained materials in constructing electrochemical aptasensors were studied, and the sensitivity detection of alpha-fetoprotein was realized.

Declaration of competing interest

The authors declare that they have no known competing financial interests or personal relationships that could have appeared to influence the work reported in this paper.

Acknowledgments

This work was supported by National Natural Science Foundation of China (Nos. U1904215 and 21471134) and Program for Innovative Research Team in Science and Technology in University of Henan Province (No. 20IRTSTHN003)

Appendix A. Supplementary data

Supplementary material related to this article can be found, in the online version, at doi:https://doi.org/10.1016/j.cclet.2020.02.044.

References

[1] A. Kirchon, L. Feng, H.F. Drake, E.A. Joseph, H.C. Zhou, Chem. Soc. Rev. 47 (2018) 8611–8638.
[2] H. Polat, M. Zeeshan, A. Uzun, S. Keskin, Chem. Eng. J. 373 (2019) 1179–1189.
[3] A. Mahmood, W. Guo, H. Tabassum, R. Zou, Adv. Energy Mater. 6 (2016) 1600423.
[4] M.Y. Masoomi, A. Morsali, A. Dhakshinamoorthy, H. Garcia, Angew. Chem. Int. Ed. 58 (2019) 15188–15205.
[5] L. Jiao, Y. Wang, H.L. Jiang, Q. Xu, Adv. Mater. 30 (2018) 1703663.
[6] Y. Xu, B. Li, S. Zheng, et al., J. Mater. Chem. A Mater. Energy Sustain. 6 (2018) 22070–22076.

[7] W.T. Koo, J.S. Jang, I.D. Kim, Chem 5 (2019) 1938–1963.
[8] Q. Wei, C. Wang, X. Zhou, et al., Biosens. Bioelectron. 142 (2019) 111540.
[9] H. An, M. Li, J. Gao, et al., Coord. Chem. Rev. 384 (2019) 90–106.
[10] Y. Zheng, S. Zheng, Y. Xu, et al., Chem. Eng. J. 373 (2019) 1319–1328.
[11] Z. Liang, C. Qu, W. Guo, R. Zou, Q. Xu, Adv. Mater. 30 (2018) 1702891.
[12] L. Ji, Y. Jin, K. Wu, C. Wan, N. Yang, Y. Tang, Anal. Chim. Acta 1031 (2018) 60–66.
[13] T. Rodenas, I. Luz, G. Prieto, et al., Nat. Mater. 14 (2015) 48–55.
[14] Y. Liu, Y. Zhang, J. Chen, H. Pang, Nanoscale 6 (2014) 10989–10994.
[15] S. Razavi, M. Masoomi, A. Morsali, Ultrason. Sonochem. 41 (2018) 17–26.
[16] C. Guo, Y. Zhang, Y. Guo, et al., Chem. Commun. 54 (2018) 252–255.
[17] Q. Zuo, T. Liu, C. Chen, et al., Angew. Chem. Int. Ed. 58 (2019) 10198–10203.
[18] H. Li, Y. Li, Z. Zhang, X. Pang, X. Yu, Mater. Des. 172 (2019) 107712.
[19] R. Marshall, C. Hobday, C. Murphie, et al., J. Mater. Chem. A 4 (2016) 6955–6963.
[20] C. Zhou, A. Li, D. Wang, et al., Chem. Commun. 55 (2019) 4071–4074.
[21] X. Dao, Y. Ni, H. Pan, Sensor. Actuat. B -Chem. 271 (2018) 33–43.
[22] A. Gheorghe, I. Imaz, J.I. van der Vlugt, D. Maspoch, S. Tanase, Dalton Trans. 48 (2019) 10043–10050.
[23] B. Ghalei, K. Wakimoto, C.Y. Wu, et al., Angew. Chem. Int. Ed. 58 (2019) 19034–19040.
[24] C. Xin, H. Zhan, X. Huang, et al., RSC Adv. 5 (2015) 27901–27911.
[25] V. Gargiulo, M. Alfè, F. Raganati, et al., Fuel 222 (2018) 319–326.
[26] M. Sindoro, A.Y. Jee, S. Granick, Chem. Commun. 49 (2013) 9576–9578.
[27] A. Knebel, S. Friebe, N.C. Bigall, et al., ACS Appl. Mater. Interfaces 8 (2016) 7536–7544.
[28] D. Liu, Y. Liu, F. Dai, et al., Dalton Trans. 44 (2015) 16421–16429.
[29] N. Zhang, X. Yang, X. Yu, et al., Chem. Eng. J. 252 (2014) 220–229.
[30] C. Zlotea, R. Campesi, F. Cuevas, et al., J. Am. Chem. Soc. 132 (2010) 2991–2997.
[31] M. Maes, L. Alaerts, F. Vermoortele, et al., J. Am. Chem. Soc. 132 (2010) 2284–2292.
[32] J. Li, H. Wei, Y. Peng, et al., Chem. Commun. 55 (2019) 7922–7925.
[33] C.S. Liu, C.X. Sun, J.Y. Tian, et al., Biosens. Bioelectron. 91 (2017) 804–810.
[34] T. Loiseau, L. Lecroq, C. Volkringer, et al., J. Am. Chem. Soc. 128 (2006) 10223–10230.
[35] Q. Liu, J.M. Yang, L.N. Jin, W.Y. Sun, Chem. Eur. J. 20 (2014) 14783–14789.
[36] S. Ahmed, X. Ding, P. Murmu, et al., Small 16 (2020) 1903173.
[37] D. Liu, F. Dai, H. Liu, Y. Liu, C. Liu, Mater. Lett. 139 (2015) 7–11.
[38] M. Wang, Y. Liu, L. Yang, et al., Sensor. Actuat. B -Chem. 281 (2019) 1063–1072.
[39] L. He, F. Duan, Y. Song, et al., 2D Mater. 4 (2017) 025098.
[40] Z. Wang, P. Dong, Z. Sun, et al., J. Mater. Chem. B 6 (2018) 2426–2431.